

Inverse-Designed Phase Prediction in Digital Lasers Using Deep Learning and Transfer Learning

YU-CHE WU, KUO-CHIH CHANG AND SHU-CHUN CHU *

Department of physics, National Cheng kung University, No.1, University Road, Tainan City 701, Taiwan

*Correspondence: scchu@mail.ncku.edu.tw; Tel.: +886-6-2757575 (ext. 65227)

Abstract:

Digital lasers control the laser beam by dynamically updating the phase patterns of the spatial light modulator (SLM) within the laser cavity. Due to the presence of nonlinear effects, such as mode competition and gain saturation in digital laser systems, it is often necessary to rely on specifically manually tailored approach or iteration processes to find suitable loaded phases in Digital lasers. This study proposes a model based on Conditional Generative Adversarial Networks (cGAN) and a modified U-Net architecture, with designed loss functions to inverse design the loaded phases. In this work, we employ deep neural networks to learn the nonlinear effects in simulated L-shape digital lasers, enabling the prediction of SLM-loaded phases for both analytical and non-analytical arbitrary structured light fields. The results demonstrate superior performance on non-analytical light fields compared to the current methods in L-shape Digital lasers. Furthermore, a transfer learning strategy is introduced, allowing knowledge obtained from one class of structured beams to be effectively reused for another, thereby enhancing generalization and improving performance under limited training data. Importantly, this method, the first proposed learning framework for digital lasers, is not limited to the L-shaped digital lasers discussed in this study, providing an efficient alternative for generating structured light in other digital laser systems.

1. Introduction

Structured light fields—laser beams characterized by specific transverse amplitude and phase distributions—play a critical role in modern optical applications. Their importance spans a wide range of fields, including optical manipulation, biomedical imaging, laser micromachining, and free-space optical communications, all of which rely heavily on precise spatial control of the light beam. Recently, Sandile Ngcobo and colleagues proposed the concept of the “digital lasers,” [1] in which a spatial light modulator (SLM) is integrated directly into the laser cavity. In this architecture, the SLM serves as one of the cavity’s end mirrors, and programmable phase modulation is used to dynamically alter the intracavity modal conditions. As a result, different laser modes and beam structures can be rapidly switched in Digital lasers without the need for replacing physical optical components. However, real-world implementations are often constrained by a variety of physical limitations. These include spatially inhomogeneous gain profiles, competitive interactions among modes [2], thermally induced refractive index variations, and nonlinear or imperfect responses from optical components such as the SLM [3]. These nonlinear and non-ideal effects introduce discrepancies between the target laser field distribution and the actual lasing mode. As a result, the ability to efficiently generate and stably maintain oscillation of structured light fields has become a key challenge in digital laser system design [4].

With recent advances in SLM technology—particularly in resolution, modulation depth, phase stability, and reflective efficiency—digital lasers have demonstrated the ability to stably

generate a wide variety of analytical beam modes, including Hermite-Gaussian, Laguerre-Gaussian, Ince-Gaussian(IG), Bessel-Gauss(BG), and Airy beams [1, 5]. These modes possess desirable features such as spatial symmetry, orbital angular momentum, and non-diffracting characteristics, making them particularly useful in precision machining and focused biomedical applications[4]. In addition to optical fields with analytical solutions, digital lasers can also generate arbitrary optical fields by appropriately controlling the SLM-loaded phase to provide the corresponding boundary phase distribution. Among the various approaches, two methods have been explicitly disclosed in the literature to implement such control. The first method, referred to as the “ $-2\phi_L$ phase boundary” [6] sets the SLM loaded phase to minus twice the target field phase, thereby ensuring that the target field is converted into its counter-propagating conjugate field upon reflection from the SLM, allowing the beam to gradually evolve toward the desired shape through round-trip propagation within the cavity [6, 7]. The second method, *Gaussian-convoluted target*, regards the target field as a non-uniformly weighted fundamental Gaussian beam and designs the $-2\phi_L$ boundary phase accordingly, producing a field that is more likely to sustain stable oscillation inside the resonator [8].

However, in digital laser systems, bridging the gap between the actual and desired output fields—particularly for non-analytical arbitrary structured light fields—remains highly challenging. The former method, $-2\phi_L$ phase boundary, theoretically supports the stable existence of the target field within the laser cavity. However, due to propagation diffraction losses and gain competition among cavity modes in the laser system, this phase boundary may lead to either stable convergence toward a field distribution that is or is not close to the intended target, or to unstable convergence, wherein the intracavity field oscillates among multiple modes. In contrast, the latter method allows all sub-Gaussian components to propagate stably but tends to overly smooth the field boundaries, resulting in loss of fine structural details. Beyond the inherent limitations of phase-projection design methods, the nonlinear characteristics of the laser system itself and imperfections in optical components also contribute to degradation of the laser quality. Consequently, methods that directly iteratively design the SLM projection phase based on the laser field have been developed [9] However, this inevitably increases the complexity of the laser system and the computation time required for repeated iterative calculation of the SLM projection phase.

Achieving high-fidelity, stable output of non-intrinsic structured light fields in digital laser systems remains challenging, highlighting the need for effective phase design methods tailored to the resonator characteristics. To address this issue, we propose an inverse design approach for SLM-loaded phases for digital lasers based on cGAN model. By utilizing dataset of loaded phases and their corresponding intracavity optical field intensities, the neural network effectively learns the nonlinear relationship between them. Additionally, the transfer learning strategies proposed in this study enable the trained cGAN model to successfully predict SLM-loaded phases for generating both analytical and non-analytical arbitrary optical fields in digital lasers. The results show that the SLM-loaded phases designed by the proposed model for generating non-analytical arbitrary structured light fields demonstrate superior performance compared with conventional methods in L-shaped digital lasers, achieving enhanced fidelity and stability in the output structured light. Importantly, this AI-based framework and deep learning strategy for phase prediction are not limited to the L-shaped architecture used in this study; in the future, they may replace iterative SLM-loaded phase design procedures and further advance the development of digital lasers for generating complex structured light.

2. Design Methods

2.1 Problem statement and Datasets Preparation: SLM-loaded Phases and Corresponding Converged Laser Fields

Fig. 1 illustrates the unfolded configuration of a classical end-pumped L-shaped digital laser [5, 6, 8, 10, 11] which can be regarded as an equivalent two-mirror resonator. One of the reflective surfaces is provided by the coated crystal facet, while the other is formed by the SLM

panel, where the loaded phase defines the phase boundary and thereby governs the laser modes generated in the digital laser. The objective of this study is to develop a deep learning model and learning strategy capable of directly predicting the corresponding SLM-loaded phase for generating a given target optical field in digital lasers.

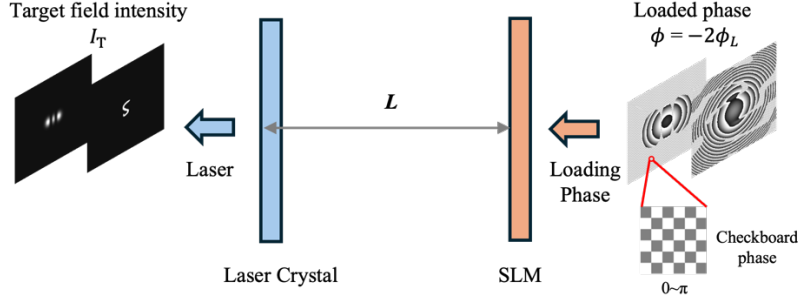


Fig. 1 An equivalent two-mirror cavity configuration for an unfolded end-pumped L-shaped digital laser.

To effectively address nonlinear effects in digital laser cavities while preserving finer spatial details of the laser fields, we generated training datasets comprising SLM-loaded phases and their corresponding laser field patterns. The SLM-loaded phases were derived using the “ $-2\phi_L$ phase boundary” method. In the main energy region of the target field, the $-2\phi_L$ phase boundary ensures that the target field is converted into its counter-propagating conjugate field upon reflection from the SLM, while a $0\text{--}\pi$ checkerboard-patterned phase was applied to the low-energy regions to increase the diffraction loss of non-target components within the laser cavity. For each SLM-loaded phase, the corresponding convergent laser fields in the L-shaped digital laser cavity were calculated using the widely adopted laser cavity convergence model proposed by Dr. Endo [5-8]. These datasets were subsequently employed to train a cGAN model for the inverse design of loaded phases corresponding to specified structured fields. The simulation parameters adopted in this study were as follows: a cavity optical length L of 24.8 cm, a lasing wavelength of 1064 nm, a Nd:YVO₄ crystal with an ordinary refractive index $n_o = 1.9573$ and a physical length of 1 mm, and a circular distribution with a diameter of 1000 μm . The cavity end mirror had a diameter of 3 mm. It is noteworthy that even though the “ $-2\phi_L$ phase boundary” physically provides a suitable phase condition to support the target light field in a digital laser cavity, it is often insufficient due to the nonlinear effects of the laser. Consequently, employing the “ $-2\phi_L$ phase boundary” in digital lasers frequently leads to two distinct behaviors during repeated intracavity propagation: (i) stable convergence to a field distribution (which may or may not be close to the intended target), or (ii) the absence of stable convergence, where the intracavity field oscillates among multiple patterns.

Based on the requirements of the subsequent study, three different types of target laser field datasets were prepared: analytically defined Ince-Gaussian modes, Bessel-Gaussian beams, and non-analytical patterns derived from MNIST handwritten digits [12], which are described in detail as follows.

a. Ince-Gaussian modes

This study chooses IG modes as representative examples, which are complete and orthogonal analytical solutions to the Helmholtz equation in elliptic cylindrical coordinates. At the $z = 0$ plane of the laser, the IG beams in elliptic coordinate system $r = (\xi, \eta)$ can be expressed as:

$$IG_{p,m}^e(r, \varepsilon) = CC_p^m(i\xi, \varepsilon)C_p^m(\eta, \varepsilon) \exp\left[-\frac{r^2}{w_0^2}\right], \quad (1)$$

$$IG_{p,m}^o(r, \varepsilon) = SS_p^m(i\xi, \varepsilon)S_p^m(\eta, \varepsilon) \exp\left[-\frac{r^2}{w_0^2}\right], \quad (2)$$

where w_0 denotes the beam waist, the superscripts e and o indicate the even and odd modes, respectively, and ε represents the ellipticity. The variables ξ and η represent the elliptic and hyperbolic coordinates in the elliptic cylindrical coordinate system, respectively, while ε is the ellipticity parameter. The terms C and S are normalization constants, whereas C_p^m and S_p^m denote the even and odd Ince polynomials. According to the modal characteristics, the mode numbers m corresponds to the number of hyperbolic nodal lines, while $(p - m)/2$ corresponds to the number of elliptic nodal lines. Consequently, $(p - m)$ must be zero or a positive even integer, since elliptic nodal lines cannot appear in half-numbers. For odd modes, $m \geq 1$ is required (at least one nodal line), whereas even modes allow $m = 0$. These modes have been well studied and are known to be stably supported in digital laser resonators [11]. By tuning the ellipticity parameter ε , IG modes continuously transform between Laguerre–Gaussian (LG) profiles ($\varepsilon \rightarrow 0$) with circular symmetry and Hermite–Gaussian (HG) profiles ($\varepsilon \rightarrow \infty$) with rectangular symmetry. We further introduced θ , representing the rotation angle of the transverse optical field coordinate grid, and constructed a dataset covering different mode parameters (*even/odd, p, m, ε, θ*). Owing to the finite effective numerical aperture of the digital laser resonator and the limited gain region size, higher-order IG modes tend to not survive in the cavity. Therefore, the ranges of the IG dataset were restricted to $p, m < 5$, with ellipticity value ε equals 1000, 5 and 0.01. In total, 576 samples were generated, each containing the light fields and its corresponding loaded phases.

b. Bessel-Gauss Beams

Bessel-Gauss beams are analytical solutions of the paraxial wave equation in circular cylindrical coordinates, which are formed by apodizing ideal nondiffracting Bessel beams with a Gaussian envelope and are characterized by a transverse intensity profile described by the Bessel function $J_m(k_t r)$. BG beams remain nearly invariant along the propagation axis z , and have been demonstrated to be stably generated in both conventional and digital lasers. [11, 13]. At the $z = 0$ plane of the laser, the even and odd BG beams in circular cylindrical coordinates (r, φ) can be divided into even and odd modes:

$$BG_m^e(r, \varphi; k_t) = \exp(-r^2/w_0^2) J_m(k_t r) \cos(m\varphi), \quad (3)$$

$$BG_m^o(r, \varphi; k_t) = \exp(-r^2/w_0^2) J_m(k_t r) \sin(m\varphi), \quad (4)$$

where k_t is the transverse wave number. The parameter w_0 is the Gaussian term waist, and the superscripts e and o denoting even and odd modes, respectively. The modal order m corresponds to the number of topological charges or radial nodal lines. We constructed a stable BG dataset by considering the stable range of BG beams within a digital laser cavity, where stable modes are defined as those that converge in the resonator, and unstable modes are those that fail to do so. Specifically, we choose the mode order m from 1 to 5 for both even and odd modes. For each mode, the corresponding stable lasing range of k_t was divided into seven equal intervals, and representative samples are collected at each boundary (including the lower limit and the upper limit). A total of 80 BG data pairs is established.

c. Non-analytical Structured Light Fields

For non-analytical structured light fields, two types of datasets were constructed based on the MNIST handwritten digits dataset [12]: (i) Stable-only, which consisted of 400 samples of optical fields that were confirmed to stably exist within the digital laser cavity; and (ii) Stable-extended, a larger dataset of 1100 samples that included the same 400 stable fields together with an additional 700 stable samples. The extended dataset was primarily designed to enhance

the model's performance on non-analytical structured light fields and to further verify its capability in predicting the loaded phases of such fields.

2.2 cGAN Model for Inverse-Designed Phase Prediction

Fig. 2 illustrates the conceptual architecture of the proposed cGAN-based inverse phase design model. The core framework adopted in this study is a U-Net generator combined with a PatchGAN discriminator, which follows the conditional generative adversarial network (cGAN) design introduced by Isola et al.[14], with further modifications in both architecture and loss functions. The U-Net architecture, originally proposed by Ronneberger et al.[15], is characterized as a fully convolutional network with a symmetric encoder-decoder structure. The encoder path comprises successive convolutional and pooling layers that progressively extract semantic representations from the input, while the decoder path employs upsampling operations to reconstruct the spatial resolution of the output. A distinctive feature of U-Net is its skip connections, which concatenate feature maps of the same resolution from the encoder and decoder, thereby enabling the integration of high-level semantic information with low-level texture details. However, as emphasized by Wang et al.[16], shallow skip connections may introduce semantic inconsistency, since resolution-matched feature maps do not necessarily share compatible semantic content. Such inconsistency can lead to output distortions or artifacts. To mitigate these issues, we strategically removed the skip connections in the first two layers of the U-Net based on empirical observations.

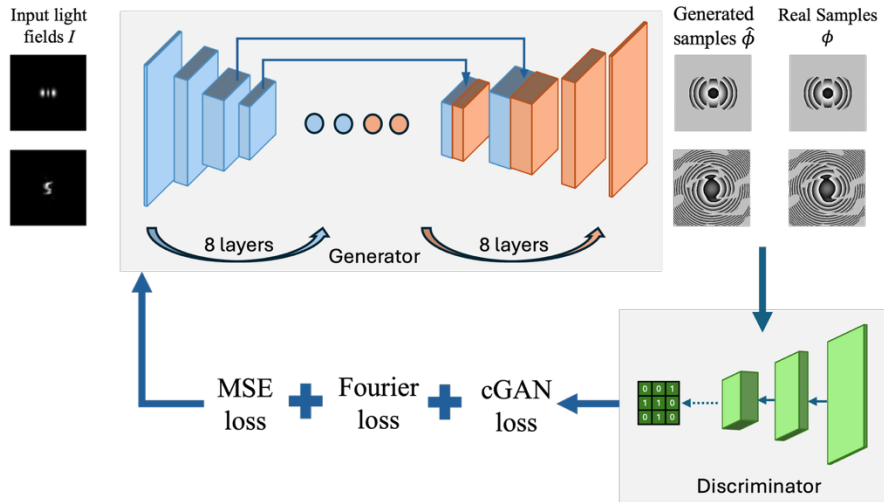


Fig. 2 Conceptual architecture of the proposed cGAN-based inverse design model. The generator (modified U-Net) maps the input light field intensity to the corresponding SLM-loaded phase, while adversarial, MSE, and Fourier losses jointly guide training.

In contrast to the standard GAN [17], which relies solely on a random noise as input, the cGAN incorporates additional information. In this work, we do not employ a latent noise vector, as output diversity is not required for the present task. Here, the light field intensity distribution I serves as the condition. The generator aims to synthesize a loaded phases $\hat{\phi} = G(I)$, while the discriminator is trained to distinguish the real pairs (I, ϕ) which are classified as true, and fake pairs $(I, \hat{\phi})$ or mismatched combinations of real light fields with incorrect loaded phases, which are classified as false. Notably, the objective of cGAN is not to perform a direct pixel-wise comparison between $\hat{\phi}$ and the ground-truth ϕ , but rather to leverage the discriminator to project the input data into a high-dimensional feature space for evaluation. To further strengthen the discriminator's ability to assess both local structures and global consistency, we also adopt

the PatchGAN discriminator architecture [14], which focuses on local image patches and outputs a confidence map that is averaged to yield the final classification score. This strategy encourages the generator to produce outputs that are locally consistent and structurally plausible. The objective function of the cGAN is defined as

$$\mathcal{L}_{\text{cGAN}}(G, D) = \mathbb{E}_{\phi, I \sim p(\phi, I)} [\log D(\phi, I)] + \mathbb{E}_{I \sim p(I)} [\log(1 - D(G(I), I))]. \quad (5)$$

Following the standard GAN training strategy, the generator was trained to minimize $-\log(D(G(I), I))$ instead of minimizing $\log(1 - D(G(I), I))$, in order to mitigate the gradient vanishing problem during the early training stage[17].

In addition to the adversarial loss, two auxiliary losses were introduced to guide the training: mean squared error (MSE) loss and Fourier loss. The MSE loss enforces pixel-level similarity between the generated phases $\hat{\phi}$ and the ground-truth loaded phases ϕ . The MSE loss is given by:

$$\mathcal{L}_{\text{MSE}} = \mathbb{E}_{\phi, I \sim p(\phi, I)} [\|G(I) - \phi\|_2^2]. \quad (6)$$

Since the MSE loss computes global differences at the pixel level, and the checkerboard pattern together with its boundaries occupy a considerable portion of the image, the MSE loss places greater emphasis on the checkerboard regions, their corresponding boundaries, and certain phase edges. The Fourier loss [18] compensates for high-frequency component loss that may occur due to encoder downsampling, consistent with the frequency-domain consistency principle. The Fourier loss is given by:

$$\mathcal{L}_{\text{F}} = \frac{1}{2} \left(\|\mathcal{F}[\hat{\phi}] - \mathcal{F}[\phi]\|_1 + \|\angle \mathcal{F}[\hat{\phi}] - \angle \mathcal{F}[\phi]\|_1 \right), \quad (7)$$

where $\mathcal{F}[\cdot]$ denotes the Fourier transform. Prior to applying the Fourier transform, a Hann window[19] was used to suppress spectral edge artifacts arising from finite image boundaries. This window gradually attenuates signal amplitude near the edges, leading to smoother transitions and more accurate spectral representation. Moreover, the Hann window suppresses peripheral checkerboard allowing the network to focus more effectively on the characteristic $-2\phi_L$ phases structural features at the phase boundary. The final objective is expressed as:

$$\mathcal{L}_{\text{total}} = \arg \min_G \max_D \mathcal{L}_{\text{cGAN}} + \lambda_1 \mathcal{L}_{\text{MSE}} + \lambda_2 \mathcal{L}_{\text{F}}. \quad (8)$$

The weighting parameters were set to $\lambda_1 = 8$ and $\lambda_2 = 0.7$, the batch size was set to 10.

Overall, the deep learning model adopted in this study followed the original cGAN framework [14] with several modifications. Since the simulated light field intensity images are inherently grayscale, the input channel dimension was set to 1. In the generator, the U-Net architecture was modified by removing the skip connections in the first two layers to reduce semantic inconsistency. The PatchGAN discriminator was simplified to three convolutional layers with 32, 64, and 128 filters, respectively. The normalization layers were all instance normalization[20], rather than batch normalization[21], to improve stability during training. Optimization was performed using the Adam solver[22], with learning rates of 0.0005 for the generator and 0.0001 for the discriminator, and momentum parameters set to $\beta_1 = 0.9$ and $\beta_2 = 0.99$. For transfer learning, continued training was adopted without reinitializing the optimizer, using learning rates of 0.0003 for the generator and 0.0001 for the discriminator.

2.3 Transfer Learning Strategy

Transfer learning enables knowledge acquired in a source task to be reused in a related target domain, which is particularly valuable when labeled data are scarce and limited [23]. Based on this concept, this study proposes a transfer learning strategy, as illustrated in Fig. 3, which shows the workflow of the proposed framework. As an initial validation, IG modes were used to demonstrate that the cGAN model can learn correspondence between structured light fields

and their associated loaded phases and be the source task. Subsequently, transfer learning strategies were applied in two representative scenarios. First, analytical BG modes were used to demonstrate that reliable prediction can be achieved with only limited data through transfer learning. Second, the MNIST handwritten digits dataset [12] was adopted as a representative non-analytical target field to demonstrate how transfer learning can improve prediction accuracy when the training datasets include poorly designed phases that fail to achieve stable laser output.

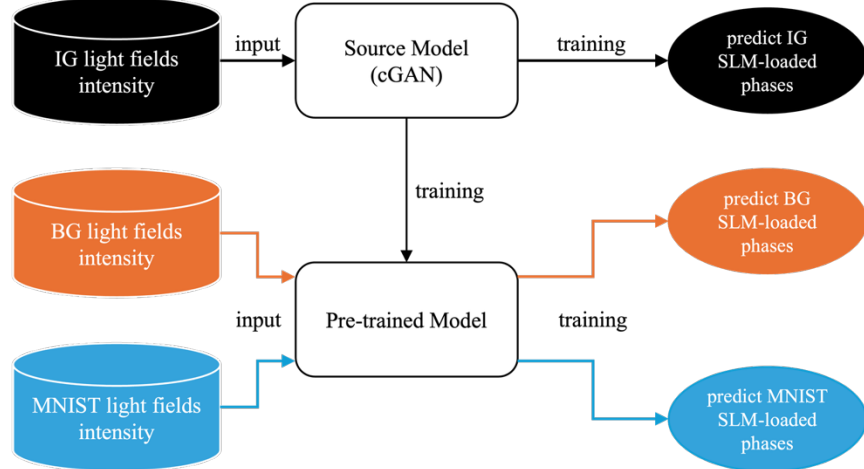


Fig. 3 Workflow of the proposed transfer learning framework for inverse-designed phase prediction in digital lasers. The cGAN model is first trained on IG modes to serve as the source model. The pretrained model is then trained with BG modes or MNIST light fields as target tasks to predict the corresponding SLM-loaded phases.

3. Results and Discussion

In this section, Section 3.1 first presents the results of the cGAN model learning, and its successful prediction of the digital laser projection phases required to generate IG modes and then demonstrates how the pretrained cGAN model, through transfer learning, can more efficiently generalize to predict the projection phases necessary for generating another class of analytical light fields, namely BG beams. Section 3.2 presents the outcomes of applying the cGAN model in combination with a transfer learning approach, highlighting its effectiveness in accurately predicting and generating non-analytical structured light in L-shaped digital laser systems.

In the following, the performance of the cGAN model, either after standard training or transfer learning, is evaluated by comparing the reconstructed light fields intensity for each test sample with the corresponding target fields intensity I_T . Two loaded phases are prepared: the loaded phases ϕ obtained via previous $-2\phi_L$ phase boundary, and the predicted loaded phases $\hat{\phi}$ generated by the cGAN model. Both loaded phases are then applied to the L-shaped laser resonator, and the resulting convergent light intensities, I (from ϕ) and \hat{I} (from $\hat{\phi}$), are computed through the simulated intracavity wave iteratively propagation modal. The similarity of I and \hat{I} with the target field intensity I_T are then evaluated separately to verify the physical plausibility and reconstruction fidelity of the predicted loaded phases. All optical field data shown below have a resolution of 256×256 pixels, corresponding to a physical area of $3.2 \text{ mm} \times 3.2 \text{ mm}$. This study uses uncentered correlation coefficient as the criteria function, which is denoted as correlation and defined as

$$\text{Correlation} = \frac{\iint [I_{\text{re}}(x, y) \cdot I_T(x, y)] dx dy}{\sqrt{\iint I_{\text{re}}(x, y)^2 dx dy} \cdot \sqrt{\iint I_T(x, y)^2 dx dy}} \quad (9)$$

where I_{re} denotes the reconstructed light field. Depending on the specific case, I_{re} may correspond either to I (from ϕ) and \hat{I} (from $\hat{\phi}$).

3.1 Validation of cGAN Model Prediction and Transfer Learning Strategy

This section presents the validation of the proposed cGAN model and its transfer learning capability. First, the effectiveness of the cGAN model is demonstrated through learning and predicting SLM-loaded phases of analytically defined IG modes. Subsequently, the pretrained model is adapted via transfer learning to predict SLM-loaded phases of another analytically defined optical field, specifically BG beams, illustrating the model's generalization across different laser patterns.

The model was first trained on the IG dataset introduced in Section 2.2 for 200 epochs. To evaluate whether the trained model is capable of predicting loaded phase to reconstruct target IG modes, 100 unseen IG mode configurations were selected as the test set. These test samples span a range of configurations (*even/odd, p, m, ε, θ*), providing a diverse distribution to evaluate the model's generalization performance on unseen data. The correlation values of the 100 testing IG samples are plotted as histograms in Fig. 4 comparing the cGAN (trained on IG modes) and the $-2\phi_L$ phase boundary method relative to the target fields I_T . The reconstructed and light intensity obtained via cGAN and $-2\phi_L$ phase boundary method of the parameter sets (e,3,1,5,3), (e,4,0,1000,177), (e,4,4,5,148), (o,4,4,0.01,148) and (o,4,2,0.01,85) are illustrated in the insets of the figure, corresponding to (a)–(e), respectively.

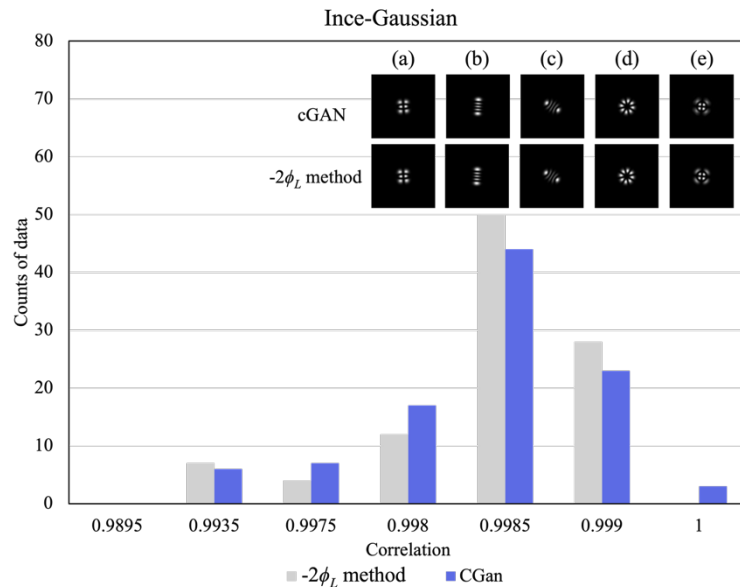


Fig. 4 Statistical distribution of correlation values for reconstructed IG light fields obtained using the cGAN (trained on IG modes) and the $-2\phi_L$ phase boundary method relative to target intensity, evaluated on 100 unseen IG configurations. Subfigures (a)–(e) show representative reconstructed fields intensity \hat{I} compared with target light fields I obtained via $-2\phi_L$ phase boundary method for parameter sets (e,3,1,5,3), (e,4,0,1000,177), (e,4,4,5,148), (o,4,4,0.01,148) and (o,4,2,0.01,85).

All test samples achieved correlation scores above 0.9895, with several exceeding 0.999, confirming that the model preserves strong spatial fidelity in predicting loaded phases for reconstructing IG light fields. These results indicate that the reconstructed light fields \hat{I} generated by the model exhibit a high degree of spatial consistency with the target fields

intensity I_T validating that the model has learned the correspondence between structured fields and their loaded phases. Moreover, the reconstruction quality is comparable to light fields intensity I obtained via $-2\phi_L$ phase boundary method, with the model outperforming it in certain cases. These findings show the model's ability in handling the learned structured IG light fields.

To further evaluate transferability under limited data conditions, we used a stable BG dataset consisting of 80 samples to train two models for 200 epochs. One model was initialized from scratch, while the other was pretrained on IG modes. We then compared their predictive capability for loaded phases of BG modes. The test set consisted of 210 unseen BG configurations (*even/odd, m, k_t*). Fig. 5 shows the statistical distribution of the correlation values of reconstructed fields \hat{I} relative to the target fields intensity I_T , comparing the BG-only training approach with the IG→BG transfer learning on the 210 unseen BG modes. The representative parameter sets (e,1,5250), (e,2,5750), (o,3,8500), (o,4,10750) and (e,5,2750) are illustrated in the subfigure, corresponding to (a)–(e), respectively.

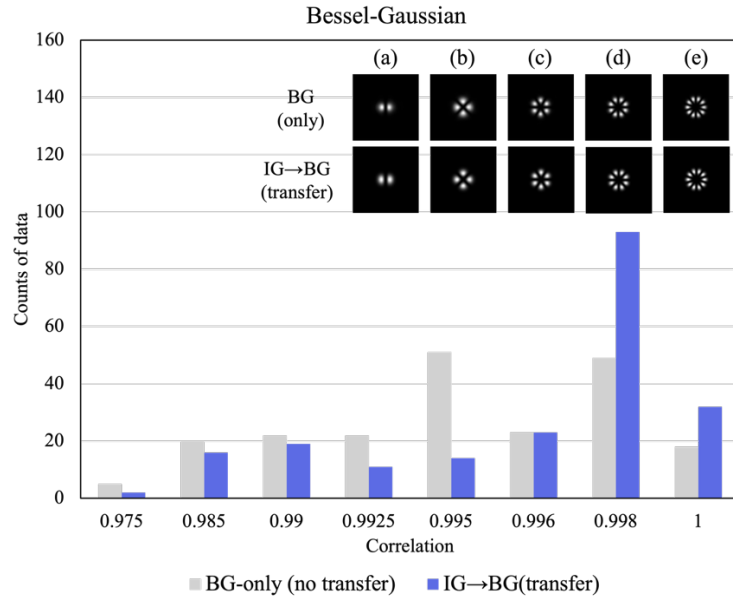


Fig. 5 Correlation values of reconstructed BG modes on 210 unseen configurations relative to the target fields intensity I_T , comparing the cGAN model trained on the stable BG dataset with cGAN transfer from IG mode to BG mode. Subfigures (a)–(e) show representative reconstructed fields intensity \hat{I} comparing the BG-only training approach with the IG→BG transfer learning for parameter sets (e,1,5250), (e,2,5750), (o,3,8500), (o,4,10750) and (e,5,2750).

For the model trained solely on BG modes it exhibits lower correlation values distribution, indicating that the model struggles to learn the characteristic features of BG beams from a limited dataset. These results reveal that, without transfer learning, the model exhibits limited generalization capability due to data scarcity, as it fails to extrapolate reliably to unseen BG configurations. In contrast, the transfer learning from IG to BG modes shifts the correlation distribution toward higher values. Although IG and BG modes belong to different modal families, they exhibit underlying structural correlations. Pretraining on IG modes thus provides physically meaningful priors, embedding essential spatial structures and resonator characteristics relevant to BG beams. Leveraging IG modes as the source task positions the pretrained model on the manifold already proximal to the BG modes solution space in latent space. With this advantageous initialization, only a few additional BG samples are needed to refine the representation and achieve accurate BG predictions. As a result, the model can

capture more robust cavity features and effectively adapt to the non-diffracting BG regime. The results demonstrate that the proposed transfer learning approach achieves improved accuracy and generalization compared with directly training the model from scratch.

3.2 Transfer learning for generating non-analytical structured light

This section presents the application of a transfer learning strategy to extend the capability of the trained cGAN model, enabling it to successfully predict the SLM-loaded phase required to generate arbitrary non-analytical optical fields in digital lasers, thereby overcoming the nonlinear effects inherent in the system and efficiently achieving stable oscillation of structured light fields.

To evaluate the model's ability to transfer to non-analytical structured light fields, we trained two models on the Stable dataset for 200 epochs: one from scratch and the other pretrained on IG modes. The test set consisted of 200 unseen non-analytical light fields, and the reconstruction fidelity was assessed using correlation. Fig. 6 shows the statistical distribution of the correlation values of reconstructed fields \hat{I} relative to the target fields intensity I_T , comparing the Stable-only training approach, and IG \rightarrow Stable transfer learning on the 200 unseen data.

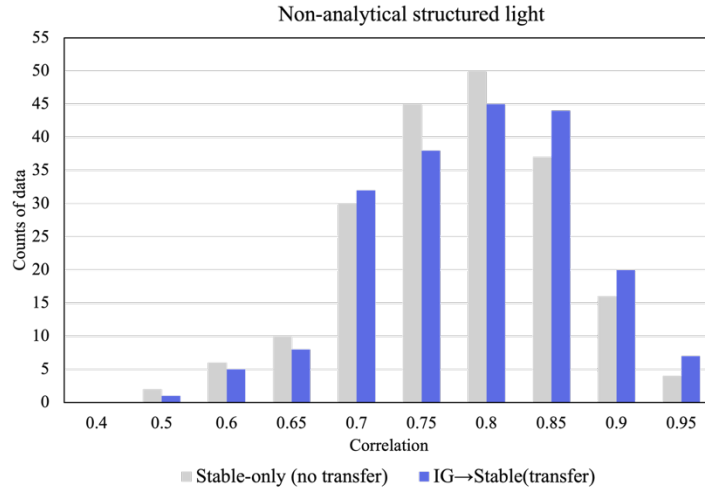


Fig. 6 shows the statistical distribution of the correlation values of reconstructed non-analytical light fields \hat{I} relative to the target field intensities I_T , comparing the Stable-only training approach with the IG \rightarrow Stable transfer learning strategy on 200 unseen samples.

As shown in Fig. 6, the model trained from scratch exhibits lower correlation values distribution, whereas the IG \rightarrow Stable transfer learning model is shifted toward higher correlation values. With transfer learning, the model outperforms training solely on the Stable-only dataset, suggesting that features learned from analytical IG modes can be effectively leveraged to improve prediction performance on non-analytical structured light fields under limited data conditions.

Fig. 6 reveals that transfer learning, even with only 400 samples, achieves reliable phase prediction for generating non-analytical light fields. To further improve the prediction accuracy of the model, we expanded the dataset to a Stable-Extended in section 2.2 and trained the pretrained model on IG modes for 200 epochs, using the same test dataset as in the previous implementation. A subsequent comparison with the conventional $-2\phi_L$ phase boundary method. Fig. 7 shows a comparison of several the reconstructed fields intensity \hat{I} of cGAN, $-2\phi_L$ phase boundary method and the target fields intensity I_T . The top row shows the reconstructed fields intensity \hat{I} from cGAN, the middle row displays the reconstructed fields

intensity I from $-2\phi_L$ phase boundary method, and the bottom row illustrates the target fields intensity I_T . Fig. 8 shows the correlation values of reconstructed fields \hat{I} relative to the target fields intensity I_T , comparing the cGAN training approach with the $-2\phi_L$ phase boundary method on the same 200 unseen dataset.

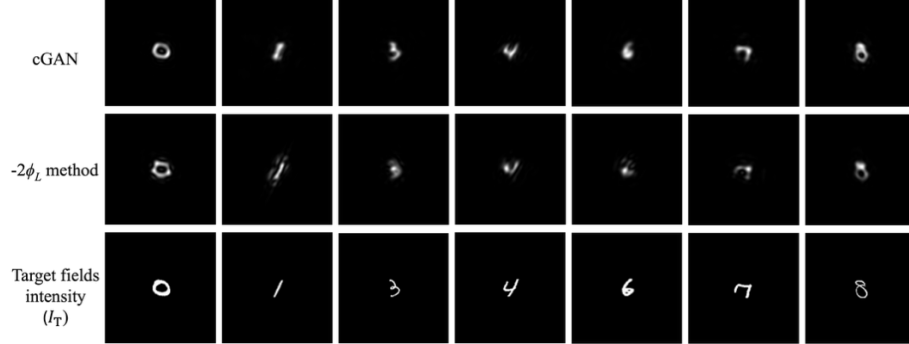


Fig. 7 Some demonstration of reconstructed fields \hat{I} of cGAN, $-2\phi_L$ phase boundary method and the target fields intensity I_T on the 200 unseen dataset.

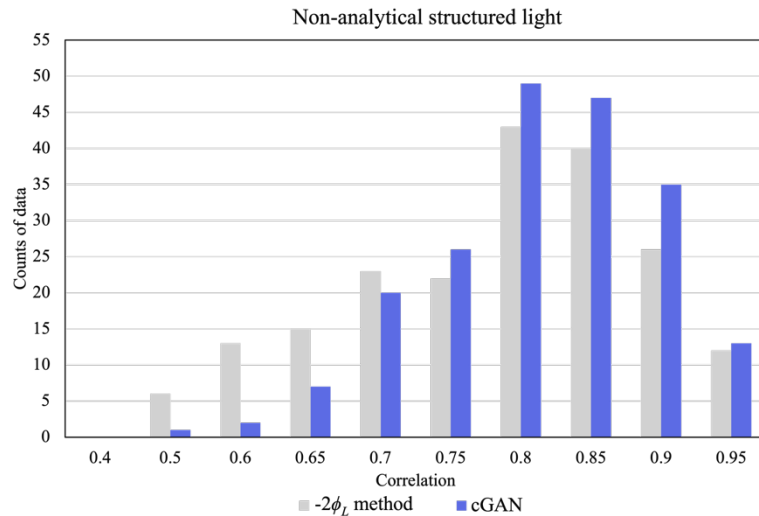


Fig. 8 Correlation values of reconstructed MNIST handwritten digits light fields on 200 unseen data relatives to the target fields intensity I_T , comparing the cGAN model transfer from IG dataset to Stable-extended dataset with the $-2\phi_L$ phase boundary method

As shown in Fig. 7, for certain target fields, the conventional method fails to converge to a stable intracavity solution or even to generate the corresponding light field. In contrast, the cGAN trained with transfer learning on the Stable-Extended dataset can successfully map these target fields to convergent loaded phases, thereby producing physically plausible and stable outputs. The implementational results highlight the limitations of the conventional $-2\phi_L$ phase boundary method. Since this approach is derived from an idealized computational phase boundary, when applied to non-analytical target fields, the nonlinear effects within the cavity or constraints on the cavity length often prevent the loaded phases from converging to a stable light field or from generating the corresponding light field. This result confirms that the deep learning model and transfer learning approach proposed in this study effectively reduce the difference between the actual and desired output fields of non-analytical, arbitrarily structured

light fields in digital lasers. The statistical results in Fig. 8 further validate this trend. The conventional method exhibits lower correlation values distribution, reflecting reduced reliability for non-analytical light fields. In contrast, the cGAN achieves higher correlations concentrated in the upper range, indicating improvements in both accuracy and reliability. These results confirm that, with sufficient training data, the cGAN can effectively capture the nonlinear effects within the cavity, thereby surpass conventional methods and enable stable reconstructions even in cases where the conventional approach fails to converge. Overall, the well-trained cGAN model can consistently predict loaded phases that enable the intra-cavity light field to stably converge to a distribution close to the intended target field intensity I_T , with its predicted phase achieving superior performance in generating non-analytical structured light fields compared to conventional methods.

Considering overall computational efficiency, the limited resolution and numerical aperture of the resonator adopted in this study inherently impose some restrictions on the performance of the digital laser, particularly because the restricted angular spectrum within the cavity further limits the spatial resolution of the generated light fields. It is therefore expected that increasing the numerical aperture of the digital laser cavity would enable the generation of light fields with higher clarity and improved spatial resolution. While the present simulations adopt a simplified resonator model, the framework is inherently scalable. A promising direction is to first train the model within numerical simulations and then transfer the learned representations to real-world digital laser systems, thereby compensating for experimental nonlinearities and imperfections. Such a simulation-to-experiment transfer pathway would enhance the practical feasibility of AI-driven inverse design.

The framework provides a data-driven nonlinear fitting approach that attempts to approximate the loaded phases capable of generating the target light fields. This characteristic complements the shortcomings of traditional theoretical methods in handling non-analytical problems and offers a new pathway for the design and control of digital lasers. Relying solely on paired intensity–phase data, the method is independent of explicit cavity parameters such as resonator length, gain region size, or pump position, thereby highlighting its versatility and showing that it is not restricted to the L-shaped configuration considered in the study. Notably, the proposed transfer learning strategy is not limited to a specific type of light field; the choice of source and target fields can be flexibly adapted according to the desired application. While this study demonstrates the framework within digital laser systems, the methodology is not confined to this domain. A wide range of end-to-end image-to-image control problems, where the mapping between structured inputs and outputs is nonlinear and difficult to model explicitly, could benefit from this type of approach.

4. Conclusion

In this study, we proposed a data-driven inverse phase design framework for digital laser systems, integrating cGAN, a modified U-Net architecture, and a composite loss function design. The framework directly predicts the SLM-loaded phase from the intended light field intensity. Trained on analytically solvable IG modes, the model achieves high-fidelity reconstructions and preserves spatial consistency with target fields intensity. With transfer learning, the pretrained model can be efficiently adapted with limited additional data to non-diffracting BG beams, outperforming models trained from scratch. Furthermore, transfer to non-analytical structured light fields such as handwritten digits patterns, demonstrating stable convergence to a distribution close to the intended targets, where the conventional $-2\phi_L$ phase boundary method often fails. These results confirm the capability of the framework to capture nonlinear effect within the laser system and provide a practical alternative to manual trial-and-error or iterative phase design processes in Digital lasers. Overall, this study highlights the potential of deep learning and transfer learning for digital lasers. Looking ahead, integrating physics-informed neural networks (PINNs)[24], the framework could evolve into a more

physically consistent model, paving the way toward robust and interpretable control of structured light fields in practical systems.

Funding. National Science and Technology Council (NSTC 114-2112-M-006-018-).

Disclosures. The authors declare no conflicts of interest.

Data availability. Data underlying the results presented in this paper are not publicly available at this time but may be obtained from the authors upon reasonable request.

References

- [1] S. Ngcobo, I. Litvin, L. Burger, A. Forbes, A digital laser for on-demand laser modes, *Nat. Commun.* 4 (2013) 6.
- [2] H. Haken, H. Sauermann, Nonlinear interaction of laser modes, *Zeitschrift für Physik* 173(3) (1963) 261-275.
- [3] R.K. Banyal, B. Raghavendra Prasad, Nonlinear response studies and corrections for a liquid crystal spatial light modulator, *Pramana* 74(6) (2010) 961-971.
- [4] A. Forbes, Structured Light from Lasers, *Laser & Photonics Reviews* 13(11) (2019) 1900140.
- [5] K.-F. Tsai, S.-C. Chu, Numerical study on the selective excitation of Helmholtz–Gauss beams in end-pumped solid-state digital lasers with the control of the laser gain transverse position provided by off-axis end pumping, *Laser Phys.* 28(3) (2018) 035801.
- [6] K.-F. Tsai, S.-C. Chu, Generating laser output with arbitrary lateral shape by using multi-point beam superposition method in digital lasers, *Laser Phys.* 28(7) (2018) 075801.
- [7] S.C. Chu, Numerical study for selective excitation of Ince-Gaussian modes in end-pumped solid-state lasers, *Opt. Express* 15(25) (2007) 16506-16519.
- [8] S.-C. Chu, Y.-X. Fu, K.-C. Chang, C.-Y. Huang, Generating a geometric structure light field from a digital laser by specifying a laser cavity phase boundary with a Gaussian-convoluted target field, *Opt. Express* 29(22) (2021) 35980-35992.
- [9] C. Tradonsky, S. Mahler, G. Cai, V. Pal, R. Chriki, A.A. Friesem, N. Davidson, High-resolution digital spatial control of a highly multimode laser, *Optica* 8(6) (2021) 880-884.
- [10] C.-Y. Huang, K.-C. Chang, S.-C. Chu, Experimental Investigation of Generating Laser Beams of on-Demand Lateral Field Distribution from Digital Lasers, *Materials* 12(14) (2019) 2226.
- [11] L.L. Nguyen Thi, K.-C. Chang, S.-C. Chu, On-demand generation of nondiffracting Helmholtz–Gauss laser beams, *Scientific Reports* 15(1) (2025) 15025.
- [12] Y. Lecun, L. Bottou, Y. Bengio, P. Haffner, Gradient-based learning applied to document recognition, *Proceedings of the IEEE* 86(11) (1998) 2278-2324.
- [13] J. Rogel-Salazar, G.H.C. New, S. Chávez-Cerda, Bessel–Gauss beam optical resonator, *Optics Communications* 190(1) (2001) 117-122.
- [14] P. Isola, J.-Y. Zhu, T. Zhou, A.A. Efros, Image-to-image translation with conditional adversarial networks, *Proceedings of the IEEE conference on computer vision and pattern recognition*, 2017, pp. 1125-1134.
- [15] O. Ronneberger, P. Fischer, T. Brox, U-net: Convolutional networks for biomedical image segmentation, *Medical image computing and computer-assisted intervention—MICCAI 2015: 18th international conference, Munich, Germany, October 5-9, 2015, proceedings, part III* 18, Springer, 2015, pp. 234-241.
- [16] H. Wang, P. Cao, J. Wang, O.R. Zaiane, UCTransNet: Rethinking the Skip Connections in U-Net from a Channel-Wise Perspective with Transformer, *Proceedings of the AAAI Conference on Artificial Intelligence* 36(3) (2022) 2441-2449.
- [17] I.J. Goodfellow, J. Pouget-Abadie, M. Mirza, B. Xu, D. Warde-Farley, S. Ozair, A. Courville, Y. Bengio, Generative adversarial nets, *Advances in neural information processing systems* 27 (2014).

- [18] D. Fuoli, L. Van Gool, R. Timofte, Fourier space losses for efficient perceptual image super-resolution, Proceedings of the IEEE/CVF International Conference on Computer Vision, 2021, pp. 2360-2369.
- [19] F.J. Harris, On the use of windows for harmonic analysis with the discrete Fourier transform, Proceedings of the IEEE 66(1) (1978) 51-83.
- [20] D. Ulyanov, A. Vedaldi, V. Lempitsky, Instance normalization: The missing ingredient for fast stylization, arXiv preprint arXiv:1607.08022 (2016).
- [21] S. Ioffe, C. Szegedy, Batch normalization: Accelerating deep network training by reducing internal covariate shift, International conference on machine learning, pmlr, 2015, pp. 448-456.
- [22] D.P. Kingma, J. Ba, Adam: A method for stochastic optimization, arXiv preprint arXiv:1412.6980 (2014).
- [23] F. Zhuang, Z. Qi, K. Duan, D. Xi, Y. Zhu, H. Zhu, H. Xiong, Q. He, A comprehensive survey on transfer learning, Proceedings of the IEEE 109(1) (2020) 43-76.
- [24] S. Cuomo, V.S. Di Cola, F. Giampaolo, G. Rozza, M. Raissi, F. Piccialli, Scientific Machine Learning Through Physics-Informed Neural Networks: Where we are and What's Next, Journal of Scientific Computing 92(3) (2022) 88.